AIMS Materials Science, 13(2): 368–390.
DOI: 10.3934/matersci.2026019
Received: 31 December 2025
Revised: 07 April 2026
Accepted: 23 April 2026
Published: 08 May 2026

https://www.aimspress.com/journal/Materials

Research article

Investigation of thermal fatigue behavior of aluminum 4032 alloy under cyclic thermal loading: An experimental study

Muhammad Arslan[1,*], Muhammad Zubair Farrukh[1,2,3], Zaheer Uddin Kamran[3] and Ahmed Usman Yasir[1]

[1] Department of Mechanical Engineering, Faculty of Mechanical and Aeronautical Engineering, University of Engineering and Technology (UET), Taxila, 47080, Pakistan
[2] Mechanical and Nuclear Engineering Department, Tennessee Technological University, Cookeville, TN, 38505, USA
[3] Department of Mechanical and Materials Engineering, University of Alabama at Birmingham, Birmingham, Alabama, 35294, USA

* **Correspondence:** Email: m.arslan5330@gmail.com; Tel: +92-312-8771440.

Abstract: Thermal fatigue is a dominant failure mechanism in aluminum piston alloys exposed to repeated heating and cooling in internal combustion engines. In this study, the thermal fatigue behavior of cast aluminum 4032 alloy (Al4032) was investigated using a custom-built test rig that combines external electrical heating with internal water cooling to generate severe cyclic thermal gradients in wedge-shaped specimens. The specimen-tip temperature was cycled between 75 and 270 °C with 10 s heating and 10 s cooling per cycle, and crack initiation and growth were monitored by optical microscopy. Thermal fatigue started cracking at approximately 3000 cycles, predominantly near the internally cooled region where the thermal gradient and associated stresses are highest. After initiation, crack length increased rapidly during intermediate cycles and then stabilized, with crack growth approaching saturation at approximately 15,000 cycles under the tested conditions. These results demonstrate that gradient-driven cyclic thermal stresses govern crack nucleation sites and subsequent propagation behavior in Al4032 and provide service-representative experimental evidence relevant to piston regions influenced by internal cooling.

Keywords: thermal fatigue; aluminum 4032; thermal stresses; crack initiation; crack propagation; crack saturation

1. Introduction

The life of any machine operating at elevated temperatures is usually governed by its thermal fatigue properties [1]. Thermal fatigue is induced by fluctuating thermal stresses, generated when a component contracts or expands due to temperature variations [2]. These stresses arise only when internal or external constraints are present [3]. Cyclic heating and cooling can impose external constraints that generate forces, while internal constraints arise from thermal gradients across the material section. Such thermal gradients are generated because heat cannot flow suddenly relative to the external temperature changes and due to differences in coefficients of thermal expansion between phases or grains [4].

Thermal fatigue initiates on the surface of the material, which expands more than the internal surface. As the internal surface is bulkier, it blocks the external surface layer from expanding, inducing compression in the internal surface layer. As heat conducts from the external to the internal layers, the external surface cools down faster than the internal surface, relieving compression stresses and generating tensile stresses at the surface. These surface stresses depend on the coefficient of thermal expansion and the temperature gradient.

Aluminum 4032 alloy (Al4032) is a high-silicon-grade alloy whose thermal fatigue life decreases with silicon modification [5]. Silicon particles significantly affect crack initiation and propagation, particularly under low strain values; their size and shape are also critical factors [6]. Increasing particle size increases stress in the matrix, while coarse particles exhibit lower yield strength than fine particles. Silicon particles with high aspect ratios are most likely to crack. If the microstructure of aluminum contains large silicon particles, then the average and peak stresses significantly increase. If the matrix yields, the chances of particle cracking increase significantly [7].

Cast aluminum alloys are mostly used in powertrain automotive components, such as cylinder heads, blocks, and pistons [8]. Light vehicle diesel engine pistons operate under cyclic temperature and combustion pressure conditions [9]. Pistons experience temperatures up to 400 °C and peak pressures up to 20 MPa, generating both thermal and mechanical fatigue, which can initiate cracks and lead to piston failure [10–13]. Most piston alloys contain 12 wt.% silicon, providing high mechanical properties at high temperatures (approximately 350 °C) [14]. Moreover, high silicon alloys are highly resistant to corrosion and abrasion. Al4032 also has a low coefficient of thermal expansion and a high strength-to-weight ratio [15–17].

Four piston alloys of Al materials, namely ACA8, SC100, A2618-T6, and A4032, can be used for manufacturing pistons. A2618-T6 has better hardness, elongation to failure, and yield strength [18]. Machines operating at high temperatures are often subjected to low-cycle fatigue and mechanical loading problems. Materials subjected to cycles of low and high temperatures are exposed to thermal fatigue, which is also known as thermal stress fatigue, creep fatigue, thermal strain fatigue, thermal cracking, thermal rupture, thermal shock, thermal endurance, heat checking, low-cycle thermal fatigue, craze cracking, heat checking, and fire cracking.

Researchers performed thermal fatigue analysis of heat-treated and non-heat-treated materials like steel, aluminum, and others [19]. For example, the thermal fatigue behavior of hot work tool steel is determined by alloy composition, particularly those with high hot yield strength and temperature resistance [20]. Cast aluminum alloy A356 exhibits different responses under thermo-mechanical loading. Heat treatment (8 h solution at 535 °C, followed by water quenching and aging for 3 h at 180 °C)

on cast aluminum has a negligible effect on low-cycle fatigue behavior, while over-aging is effective on plastic strains, leading to increased material life [21].

Aluminum alloys are easily affected by environmentally assisted fatigue crack propagation (EAFCP), particularly in aerospace construction. Some protective coatings contain inhibitors to mitigate this issue. The EAFCP has been investigated on AA2024-T3 aluminum alloy in a 3.5% NaCl solution containing different levels of chromate inhibitor, and fatigue tests were carried out on center-cracked tension (CCT) specimens in a longitudinal–transverse direction. The solution reduced the corrosion rate and inhibited EAFCP due to the passive films acting as a wall for hydrogen diffusion, also called reducing hydrogen embrittlement into crack tips. As inhibitors (chromate) increase, EAFCP is gradually reduced. The effect of low-cycle fatigue (LCF) was observed on two types of aluminum grades, namely 2024 and 7075, under different heat treatments at room temperature [22], with LCF parameters (strain ratio of -1 and frequency of 5 Hz) and three environments: vacuum, air, and a solution of 1% NaCl. LCF was also tested on specimens pre-corroded in 1% NaCl. LCF was observed to be lowest in vacuum, highest in 1% NaCl, and moderate in air. LCF was not significantly affected by the ambient air.

Thermal fatigue has also been investigated on copper-plated Al2024 and uncoated Al2024; copper was diffused into the middle of the surface. Age hardening can increase fatigue performance by 34%. Heat treatment effects on the microstructure of Al2024 and fine precipitates showed increased fatigue life, whereas copper plating weakened the material and reduced fatigue life [23]. During internal cooling and external heating, with and without applying axial force on the specimen, there were no cracks between 300 and 400 °C. Cracks usually propagate at 500 °C, at which point specimens fail. It was also noted that axial cracks formed without load, while circular cracks formed when axial load was applied on a 316L steel pipe [24].

Thermal fatigue is also affected by hardness, as observed in the American Iron and Steel Institute (AISI) H13 tool steel, where increased hardness reduces crack growth rates. However, research shows that heat treatment has a negligible effect on crack growth; numerical studies using finite element method (FEM) have focused on thermal fatigue (TF) and thermomechanical fatigue (TMF). The life of a piston can be predicted using different fatigue criteria; constant fatigue loading is used in conventional fatigue criteria, while variable amplitude fatigue loading is important for life prediction. Miner's linear accumulation rule has been widely used for fatigue life prediction [25,26]. Mechanical fatigue at different temperatures significantly impacts cast magnesium alloy fractures. At room temperature, the fracture shows cyclic hardening behavior, whereas at high temperature, AZ91 magnesium alloy shows a brittle fracture. Moreover, fatigue life is greater at high temperatures than at low temperatures [27].

Three main piston manufacturing techniques are used: casting, forging, and sintering. Casting is the most popular technique, even though cast materials have a more fragile microstructure and worse dimensional accuracy. The tensile strength of a powder-forged piston is double that of a cast piston. A forged piston is better for crack and shock loads [28]. A356-T7 aluminum alloy is used in diesel engine cylinder heads, whose operating temperature may exceed 230 °C, and a negative minimum temperature may produce thermal strain. Therefore, a strain crack can initiate and propagate, which leads to the failure of the cylinder head. Mostly, crack propagation depends on K_{max} and temperature at low and high frequencies. A diesel piston mainly operates at high temperature and pressure conditions (e.g., 400 °C and 20 MPa). The peak temperature of 400 °C corresponds to the combustion-exposed temperature of the piston crown. On the other hand, due to oil galleries and heat dissipation through the piston body,

the temperature within the subsurface region and near the internal cooling channel is significantly lower. These regions typically experience cyclic temperature variation within a moderate range but are subjected to steep thermal gradients due to simultaneous heating and cooling effects.

Since thermal fatigue is primarily driven by temperature gradients rather than temperature alone, the present study focuses on a temperature range of (75–270 °C) to simulate the thermal conditions experienced near internally cooled regions of piston components. Pure aluminum has a high coefficient of thermal expansion; therefore, pistons cannot be cast from pure aluminum, and silicon and other elements like Cu, Ni, and Mg are added to reduce thermal expansion [11]. Mostly, fatigue cracks initiate in cast piston alloys at silicon particles at ambient temperatures of 200, 300, and 350 °C) [9,12–14]. The orientation of welding has a significant impact on crack initiation and propagation. Crack mainly initiates at the interface between the weld and the base metal. The response of crack propagation on the interface between the base and the weld metal is quick but slows down as the number of cracks increases [29]. The thickness of the specimen has no significant effect on thermal fatigue life. Different thickness sheets (0.91–1.2 mm) of the polycrystalline nickel-based super alloy 263 have been investigated for thermal fatigue life at specified conditions (heating temperature 900 °C, cooling temperature 50 °C, and 2 min cycle time, 290–300 cycles) [30]. The T6 heat treatment showed considerable effects in increased mechanical properties and LCF of A356 aluminum alloy, but a negligible effect on TMF loadings. With an increase in the temperature range, the difference between the lifetime of A356 and A356-T6 alloys decreases [21]. A splash cooling system, used in 1985 and by Amiable, Chapuliot [31], of approximately 600 °C/s, resulted in a crack network starting after approximately 100,000 cycles in 304 stainless steel material. Thermal fatigue was investigated on different types of experimental setups or rigs. For example, for thermal fatigue analysis of a diesel piston, a heating coil was used for heating the piston crown at 100–300 kHz during continuous cooling from the inside of the piston at 20 °C at a flow rate of 10 L/min [32]. An experimental rig was used for cyclic internal cooling and external heating to check crack initiation and propagation in the specimen. The outer surface was heated at 300–500 °C for 40–45 s, followed by water quenching for 5 s at room temperature. A coil was used for heating, and an internal bore was used for cooling. Axial forces of 50 and 100 kN were also applied on the uncracked specimen, providing 33 and 66 MPa stresses [33]. For thermal fatigue analysis of the H13 steel, rods were used, which consumed 1500 W of power in a furnace to achieve a temperature of 750 °C; cooling was achieved by forced air to 25 °C. Heating and cooling times were kept at 240 and 120 s, respectively [34]. A stainless steel 316L pipe was investigated for thermal fatigue. Cold water was cyclically sprayed inside the specimen pipe. For outside heating of the specimen, a furnace was used [35]. In [36], an experimental setup was used for testing LCF and TMF, where a coil was used for induction heating for maximum values (e.g., 200–275 °C). To cool down to 50 °C, compressed air was used through a compressed air jet system. All experiments were set to 10 °C/s. In [30], a splash system was used for the cooling cycle during thermal fatigue analysis of a 304 stainless steel material. A parallelogram geometry specimen with dimensions of 200 × 30 × 20 mm was subjected to heating on one face and cyclical cooling by water spray on the opposite face at a localized zone (10 × 5 mm). Cooling and heating times for this setup were 0.25 and 7.5 s, respectively.

The innovativeness of the present study lies in the purely experimental, service-representative evaluation of thermal fatigue behaviors in a Al4032 alloy using a controlled cyclic thermal loading approach that closely mimics piston operating conditions. Although the literature on thermal fatigue of metallic materials is quite comprehensive, some significant limitations remain. Most previous

investigations were based on simplified thermal loading conditions, including uniform heating, isothermal fatigue, or combined thermo-mechanical simulations, which are not relevant to the harsh thermal gradients that occur in actual piston components. Specifically, the combined influence of internal cooling and external heating, which leads to the creation of sharp temperature contrasts in service, is not often recreated in controlled laboratory environments. Moreover, many works have focused on crack initiation or fatigue life prediction, with little experimental research on the entire development of thermal fatigue damage, including the start, growth, and interaction of the crack, and saturation behavior. To fill these gaps, the current study constructs an experimental system specifically designed to provide external heating and internal cooling of wedge-shaped specimens, creating realistic cyclic thermal gradients that resemble piston working conditions. In contrast to traditional methods, this work offers purely experimental research on the nature of thermal fatigue in Al4032, including a detailed description of crack initiation, propagation, and saturation stages. This paper thus helps to fill the gap existing between simplified laboratory tests and the real service environment, providing a more credible understanding of the thermal fatigue behavior of piston alloys. This experimentally driven insight offers a more reliable basis for assessing material durability under real operating environments and contributes original knowledge toward improving the thermal fatigue resistance of aluminum-based engine components.

2. Materials and methods

A thermal fatigue experimental setup was designed and fabricated for thermal fatigue analysis of different alloys, i.e., aluminum, copper, and different low-melting materials. For thermal fatigue purposes, cyclic heating and cooling were applied to the wedge-shaped specimen. A constant-temperature milled steel tab was provided for heating purposes. The wedge-shaped specimen was in contact with a drilled hole on the tab. Four electric rod filaments were attached around the tab. These electric filaments were controlled with a thermocouple controller to maintain the required constant temperature. Heat transfer to the specimen was achieved through direct contact with the heated steel tab. The heating system was controlled using a thermocouple-based feedback mechanism to maintain the desired temperature at the heating tab. Consistent mechanical contact between the specimen and the heating surface was ensured using a spring-loaded mechanism throughout all experiments. This arrangement allowed limited freedom for thermal expansion while maintaining stable contact. No external mechanical load was applied; however, minor contact forces and frictional interactions may have existed at the interface. The system was operated under steady-state conditions to ensure consistent thermal input during the experimentation. Temperature was measured using a K-type thermocouple positioned near the specimen tip. This provides local temperature history for cycle control. For temperature measurement, a K-type thermocouple (OMEGA Eng.) with an accuracy of ±0.5 °C was used. Prior to experimentation, thermocouples were calibrated using a two-point calibration method: an ice water bath at 0 °C and controlled boiling water at 100 °C under local atmospheric pressure. The maximum deviation observed after calibration was within ± 0.3 °C. Each rod consumed 1000 W and generated an electric flux, heating the tap, as shown in Figure 1.

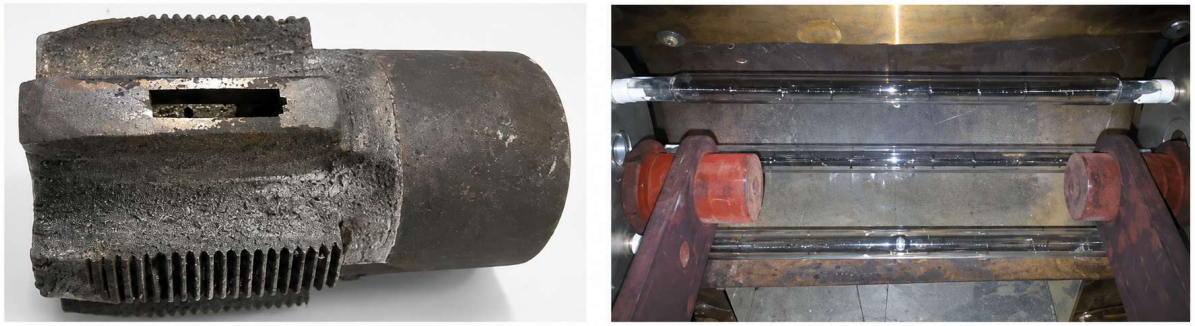

(a) (b)

Figure 1. (a) Heating tab and (b) heating filaments.

Internal cooling was achieved by circulating water through the specimen at a controlled flow rate. The coolant temperature was maintained at 25 °C, and flow regulations were achieved using a bypass valve. The system was operated under steady-state conditions, repeated for all tests. For cooling purposes, the water tank was used inside the frame, and an electric motor (water pump) was used for the circulation of water inside the specimen. A bypass valve was used in the circulation of cooling water to regulate the cool water. Specifications of the water pump are given in Table 1.

Table 1. Specifications of the water pump.

Power	Voltage	Current	Frequency	Max. head	Max. section
0.45 kW	220 V	3 A	50 Hz	50 m	18 m

The flow rate of cooling water from the specimen was set to 555 mm^3/s. The cooling water flow rate was regulated using a bypass valve to maintain a stable flow during testing. Minor fluctuations in flow could have occurred due to the pump operation; still, the overall system operated under steady-state conditions throughout all experiments to ensure consistency.

High temperature and electricity can damage the sliding bars, electric connectors, and protection plate. The compressed air-cooling system was used primarily for thermal protection of the system components and stabilization of the experimental environment. Airflow conditions were kept constant during all experiment runs. To protect all components, a blower with distribution pipes was designed and installed on the experimental rig. The blower cooled down the setup to the minimum possible temperature. The specimen, together with its holder, can slide on two sliding bars in a "to-and-fro motion" for specified cooling and heating, in which the edge of the specimen is continuously attached or detached from the tab for a specified time. A stepper motor was used for sliding the specimen holder using linkages and rods. A spring was used to properly attach the specimen to the tab so that heat was transferred through conduction. To investigate crack initiation and propagation, optical microscopy (Optika Microscope Italy) was used. The Stereo Zoom Microscope (SZM) is a high-performance microscope with a continuous zoom system of 0.67–4.5× and widefield high-point 22 mm eyepieces. An Arduino Uno R3 was used, and a complete electronic circuit was developed for controlling stepper motors. The electric circuit included Arduino UNO R3, H-Bridge L298, stepper motor, push button, Max 6675, K-type thermocouple, and a power supply. The experimental setup is shown in Figure 2.

Figure 2. Experimental setup.

2.1. Specimen preparation and material testing

Aluminum was used for thermal fatigue analysis in this research. The test material was aluminum alloy 4032 as it is commonly used in piston components of automotive engines under cyclic thermal loading. The samples in the current research were made using a traditional casting path. A large pattern of wood was used to produce a series of specimens, which were post-cast machined to the final geometry needed to test thermal fatigue. The alloy was melted at 800 °C and was allowed to stay at this temperature for approximately 10 min to be fully melted and sufficiently fluid to cast. The hot molten metal was then cast into ready molds to produce wedge-shaped castings. The cast specimens were removed after solidification and subjected to machining processes such as milling, drilling, and grinding to obtain the desired sizes and surface finish, as indicated in Figure 3. Dimensional consistency between specimens used in the experimental program was taken into consideration. For microstructural-level characterization, standard metallographic preparation was used. Surface irregularities and deformation layers on the specimen surfaces were first ground with silicon carbide (SiC) abrasive papers of gradually finer grit size (400, 800, 1200, 1500, and 2000) under water lubrication. Polishing was then carried out with a decreasing particle size (6, 3, and 1 μm) of diamond paste placed on a trident cloth to achieve a mirror-like finish to the surface of the polished material that could be analyzed under the microscope. Etching was conducted using two reagents to demonstrate different microstructural characteristics of the cast alloy: Keller's reagent was used to observe dendritic structures and dendrite arm spacing (DAS), and Weck's reagent was used to observe the eutectic phases and silicon morphology under polarized light. Tables 2 and 3 provide the compositions of the etchants. Etching was performed very selectively to prevent excessive etching and to provide distinct microstructural contrast under optical microscopy. Four patterns were used for the preparation of specimens, as shown in Figure 3a. After casting, specimens were machined for accurate dimensions, as given in Figure 3b. Different machining processes were involved for preparation, such as milling, drilling, and grinding.

(a) (b)

Figure 3. (a) Casted specimen and (b) finished specimen.

Table 2. Composition of Keller's etchant.

Chemical composition	Quantity
Water	95 mL
HNO_3	2.5 g
HCl	1.5 g
HF-immerse	1.0 g
Immersion duration	10 s

Table 3. Composition of Weck's etchant.

Chemical composition	Quantity
Water	100 mL
$KMnO_4$	4 g
NaOH	1 g
Immersion duration	20 s

The OLYMPUS BX51 metallurgical microscope was used to investigate the grain boundaries of the cast aluminum. The dendritic microstructure of casted Al4032 is shown in Figure 4.

Figure 4 shows DAS at different magnifications for the as-cast aluminum. As per the ASTM standard book Metallography and Microscopy, Volume 9 [34], as-cast aluminum 4xxx series enriched with Si exhibits four morphologies, namely Si, Al_2Cu, β-AlFeSi, and α-Al (FeMnSi), without heat treatment. Weck's etchants are mostly used to investigate hypereutectic as-cast aluminum, eutectic α-Al, and Si, and are viewed with polarized light. Weck's etchant is easy to use and provides good results for cast aluminum.

Figure 4. Microstructure of Keller's etchant at different magnifications.

Al4032 is a silicon-rich alloy, with different phases of Si, β-AlFeSi, and α-Al (FeMnSi) with polyhedral, branched platelets, rods, or Chinese script morphologies [34]. The Si phase usually shows polyhedral or branched platelet morphology. Figure 5 shows the optical micrograph of Al4032 etched with Weck's reagent, showing the α-Al matrix and Si-rich eutectic regions. The bright/light regions correspond to the α-Al matrix, while the dark/contrasting regions correspond to eutectic Si/Si-rich phases (as revealed under polarized light). β-AlFeSi and α-Al (FeMnSi) have needle-like and Chinese script morphology, respectively. A scanning electron microscope (SEM) was used for testing and scanning the composition of Al4032. Images taken by SEM at different magnifications are given in Figure 6.

The observed thermal fatigue crack initiation behavior can be directly correlated with the microstructural characteristics of the cast Al4032 alloy. Crack length measurements were obtained using an optical microscope. The uncertainty in crack length was estimated to be within ±10–20 µm.

This uncertainty does not significantly affect the observed trend of crack growth over the number of thermal cycles.

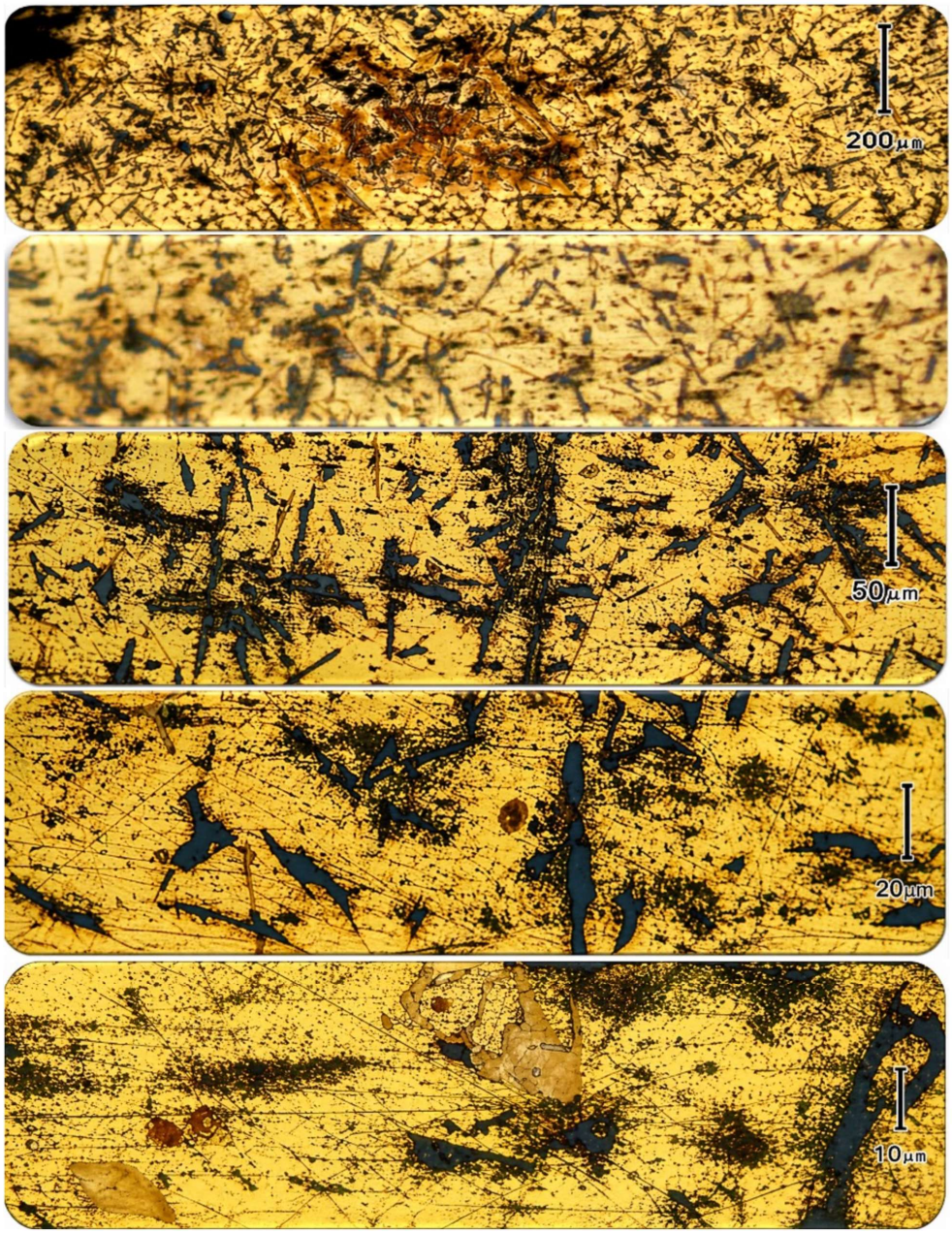

Figure 5. Eutectic regions of α-Al and Si.

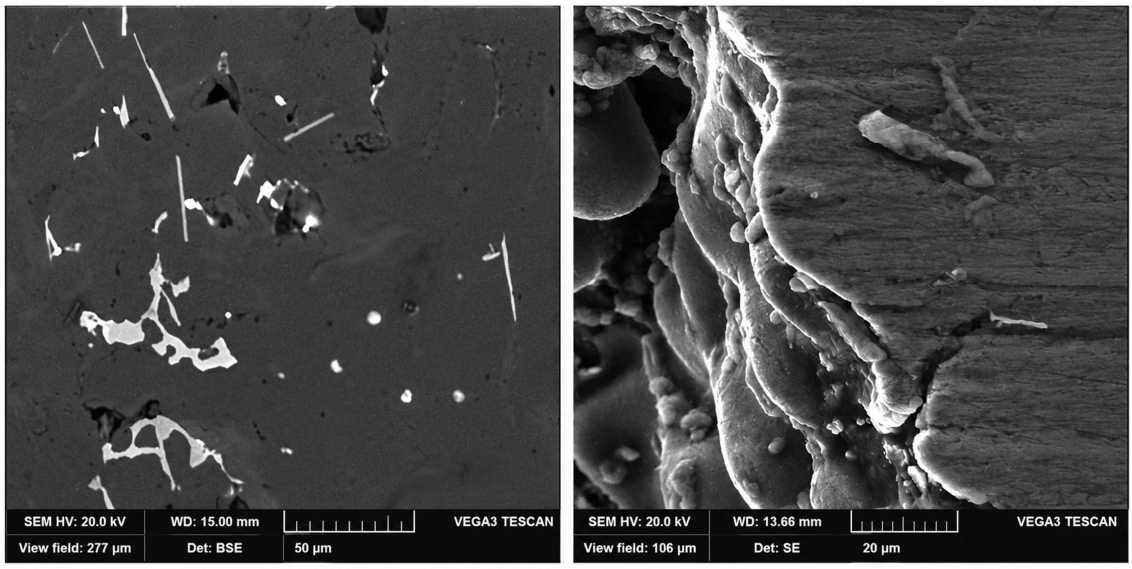

Figure 6. SEM images of Al4032 at (a) 500× and (b) 1380×.

The microstructure, as revealed by optical microscopy and SEM analysis, consists of an α-Al matrix embedded with Si particles and intermetallic phases such as Al_2Cu and Fe-containing compounds. Due to a significant mismatch in the coefficient of thermal expansion between the ductile aluminum matrix and relatively brittle silicon particles, cyclic thermal loadings include localized interfacial stresses at the matrix–particle boundaries. During heating and cooling cycles, the aluminum matrix undergoes larger volumetric expansion and contraction compared to silicon particles, resulting in stress accumulation at these interfaces. In addition, the morphology and size of silicon particles play a critical role in crack initiation. Coarse and angular Si particles, as observed in the as-cast microstructure, act as stress concentrators and preferential sites for microcrack nucleation. These particles are unable to accommodate plastic deformation effectively, leading to early fracture under cyclic thermal stresses. The presence of intermetallic phases such as Al_2Cu and Fe-rich phases further contributes to microstructural heterogeneity, promoting localized stress intensification and facilitating crack initiation. Once initiated, microcracks propagate along paths of least resistance, often following particle–matrix interfaces or linking adjacent brittle phases. The combined effect of thermal expansion mismatch, brittle particle fracture, and heterogeneous phase distribution leads to the formation of crack networks observed during the propagation stage. This microstructural mechanism explains why crack initiation predominantly occurs in regions subjected to high thermal gradients, where thermal stresses are maximized, and microstructural incompatibilities are most severely activated.

Al4032 is used in pistons due to its enrichment with silicon. It has low thermal expansion while working at high temperatures. The chemical composition of the specimens tested by SEM is shown in Figure 7.

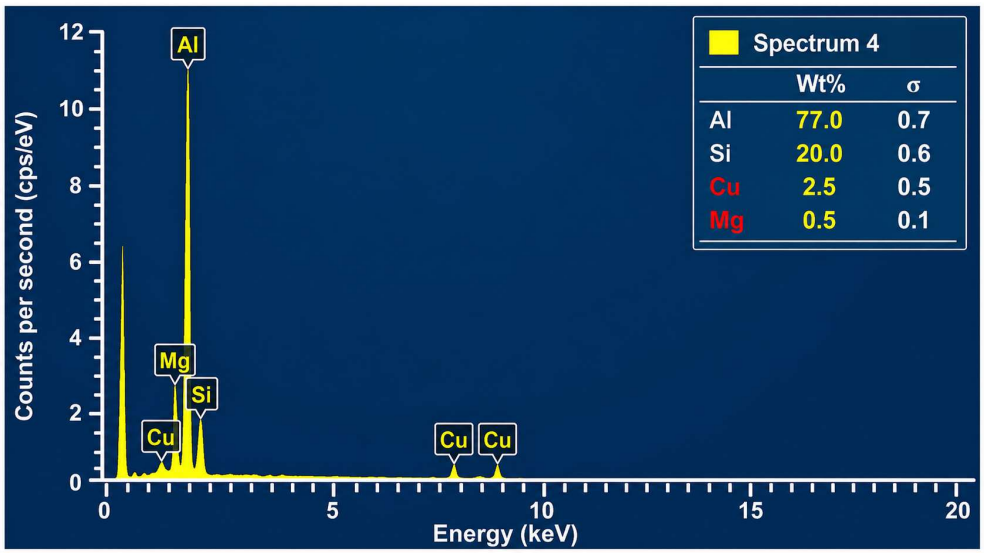

Figure 7. Chemical composition of Al4032.

Tensile tests were carried out on an MTS machine (model 810). For tensile testing, a standard specimen of cast Al4032 was followed [35]. The stress-strain curve shown in Figure 8 was obtained from the MTS test. These mechanical tests are included to provide contextual support for the cast material state; the main conclusions of this paper are drawn from thermal-fatigue crack evolution under controlled thermal cycling.

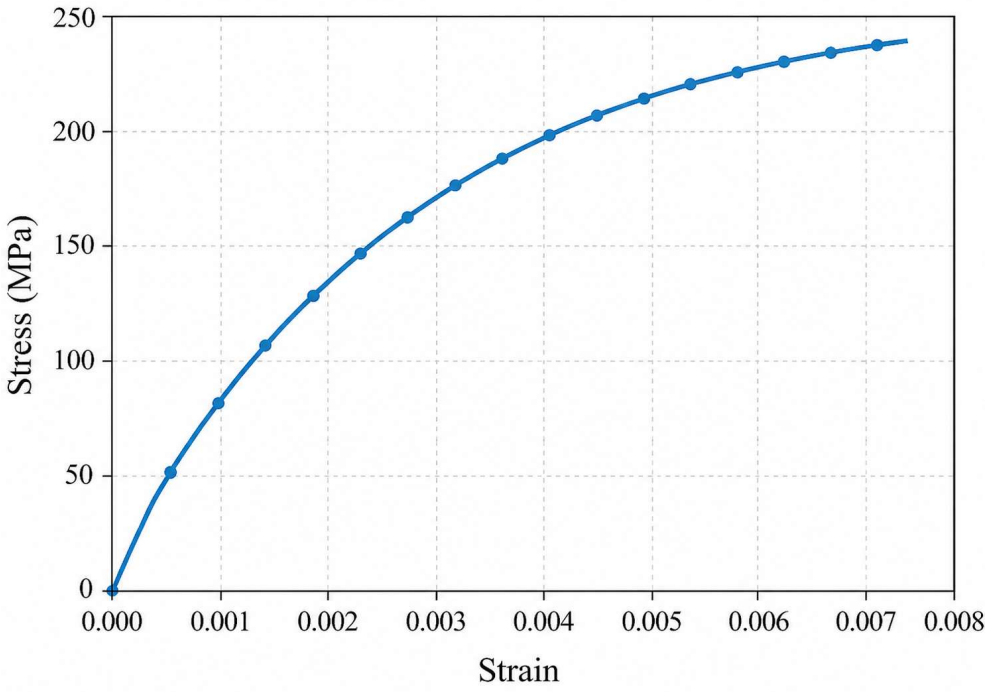

Figure 8. Stress vs. strain curve for Al4032.

3. Results and discussion

Experiments were carried out on a fabricated thermal fatigue rig. Two cooling systems were installed in the experimental rig. One cooling system was for specimen's internal cooling, where water was used for cooling at a flow rate of 100 mm^3/s, and water temperature was kept at 25 °C. Water flow of water could be controlled by a bypass valve that slightly changes the flow rate. The second cooling system was installed on the rig cooling back plate of the tab. This tab plate was cooled by compressed air; a blower was used to supply compressed air, and pipes were used to direct this air toward the tab plate and electric connectors. The tab temperature was controlled by a temperature controller. A thermocouple was connected to the temperature controller, which senses the tab temperature. The cutoff temperature was set by the temperature controller. Different temperatures were set (e.g., 400, 500, and 600 °C). The servo motor moved the specimen back and forth, which cyclically heated and cooled the specimen tip, while the back of the specimen remained at constant temperature. To obtain the temperature of the specimen tip, a k-type thermocouple was mounted 1 mm from the tip. For mounting the thermocouple, a 1 mm hole was drilled in the specimen. This thermocouple continuously provided readings. By increasing heating and cooling time, maximum and minimum temperatures were also increased, but further increases in time provided a constant temperature curve. To increase specimen temperature, the tab temperature could be increased; however, there were some limitations in the design of the rig for increasing the temperature. At the same time, by decreasing the temperature of the cooling cycle, the temperature of the water must be kept low. The temperature of the specimen reaches a steady-state condition after a few hundred cycles. The thermal cycling waveform consists of alternating heating and cooling phases, each lasting 10 s, resulting in a periodic thermal cycle. The specimen tip temperature varied between 75 and 270 °C. No isothermal holding stage was applied, and heating and cooling rates were governed by the thermal response of the system under these controlled time intervals. The experimental temperature cycle is shown in Figure 9.

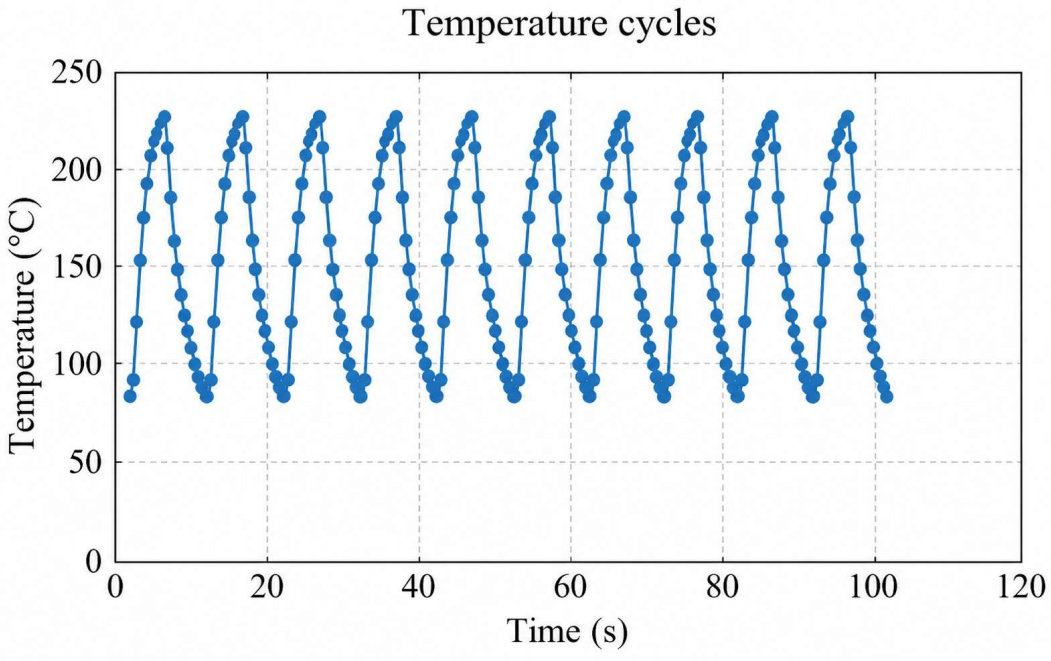

Figure 9. Ten temperature cycles.

The temperature range is consistent with subsurface thermal conditions in piston components subjected to internal cooling, where thermal gradients are more critical than peak surface temperatures in governing fatigue damage. This graph shows steady-state conditions of the specimen temperature. One edge of the specimen, being wedge-shaped, cyclically bears thermal fatigue in the range of 75–270 °C. Heating and cooling times were kept to 10 s. The tip of the specimen was tested after every 500 cycles using the Optika Microscope Italy. Cracks could only be seen when they reached up to 300 μm. Additionally, an oxide layer can also form, which affects the detection of cracks under the microscope [25]. Cracks can be observed during initiation, propagation, and saturation. Cracks in Al4032 were observed after approximately 3000 cycles under the tested conditions. During the propagation stage (the main stage) crack depth is sharply increased. In Al4032, crack growth was observed to stabilize after approximately 15,000 cycles. Afterward, crack propagation ended, and crack length remained constant with increasing cycles. This stage is called crack saturation, as shown in Figure 10.

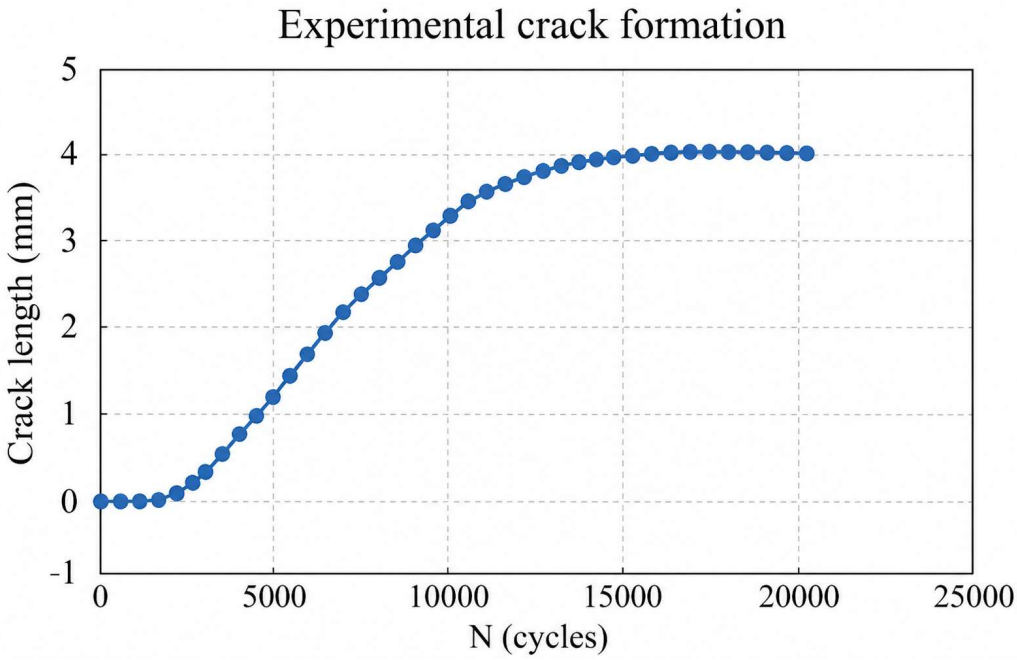

Figure 10. Crack length vs. cycles.

The specimen was designed to minimize external mechanical constraints; however, minor contact and fluid-induced effects may be present. Under the applied cyclic heating and cooling conditions, thermal stresses are expected to be the dominant contributors to crack initiation and propagation. If a graph is drawn between stress along tips, cycle time, and temperature, the stress profile follows the temperature profile, as shown in Figure 11.

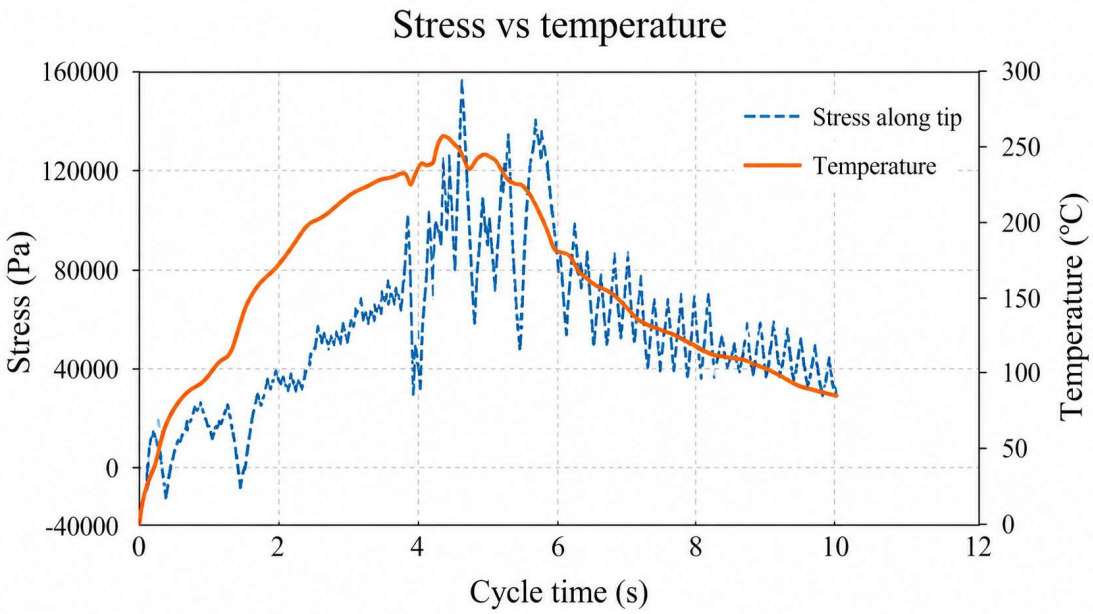

Figure 11. Stress vs. temperature.

As the stress fluctuates with the temperature, minor changes in temperature can abruptly change the stress. During heating, stress increases at a lower rate than temperature, due to the time taken by the specimen to attain a steady-state condition. During cooling, both stress and temperature have the same profile, and stress decreases at the same rate as that of temperature. This stress causes crack initiation and propagation. A 3D stress graph can be drawn along the specimen tip and depth, as shown in Figure 12. This graph shows that the maximum stress is on the side of internal cooling. Water has maximum cooling in the middle; therefore, thermal stresses are generated in the middle portion of the tip rather than at the corners.

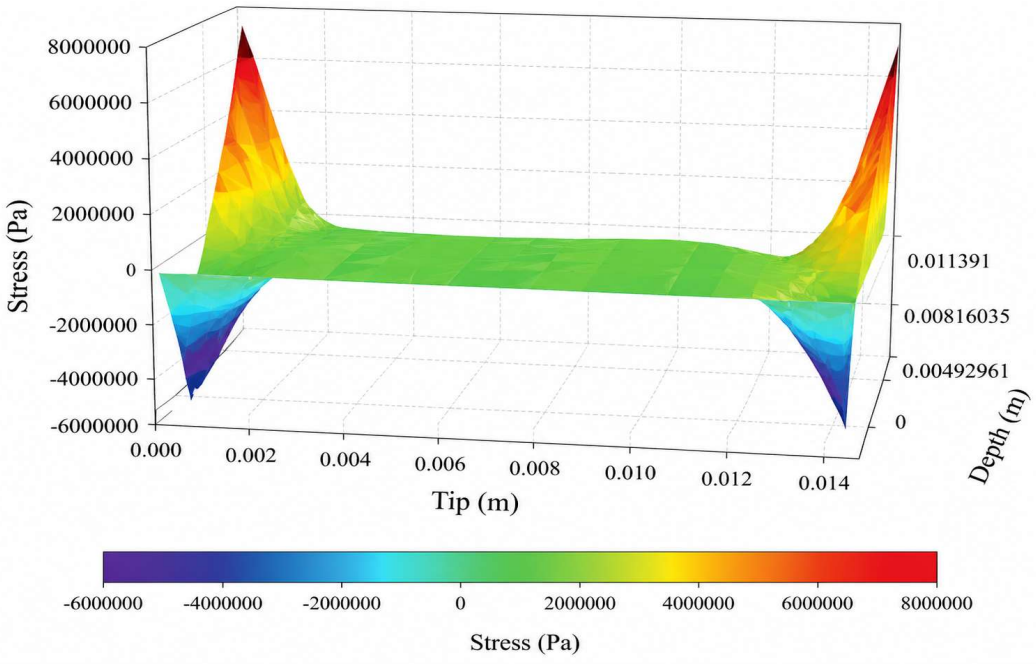

Figure 12. 3D stress along the tip and depth.

Water cooling stresses were highest in two portions, from 3.3533 to 5.3 mm from the corner on both sides of the specimen. The peak stress along the tip was 76.4 kPa, and in the center, the stress was 60 kPa. Crack initiated in the regions of maximum stress. Figure 13 shows the stress at the tip in the S11 direction, clearly showing that stress was lower in the center than at some distance from the sides.

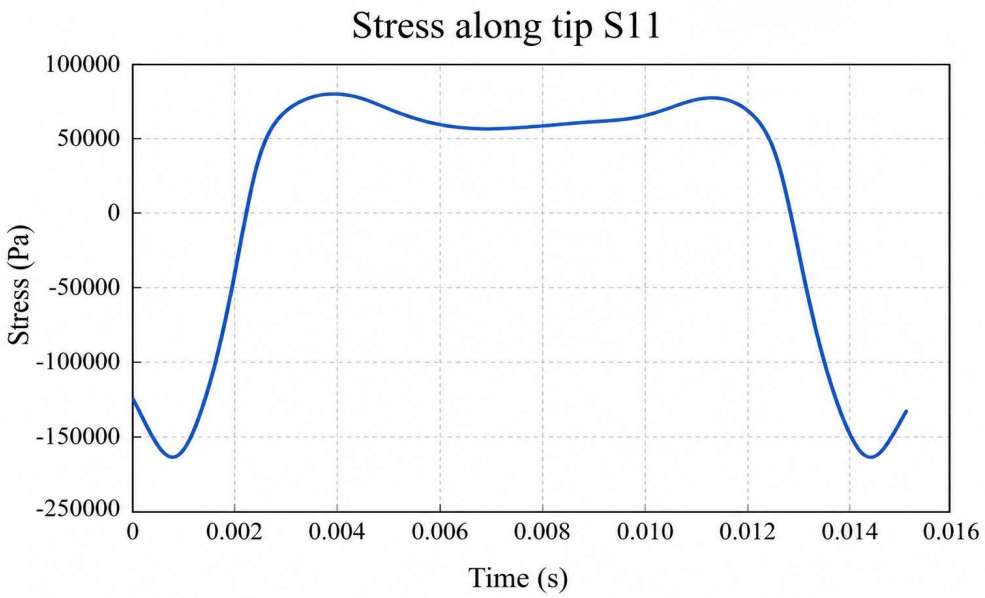

Figure 13. Stress along the specimen tip.

Stress at 4.4 mm from the tip remained constant in depth for 4.1 mm; after that, stress reduced. This means that the crack propagated only approximately 4.1 mm. Figure 14 shows that the stress increased along depth at approximately 4.12187 mm at a middle path depth of approximately 7.067 mm. After approximately 6.54501 mm, the stress was compressive; as such, the crack could not propagate further.

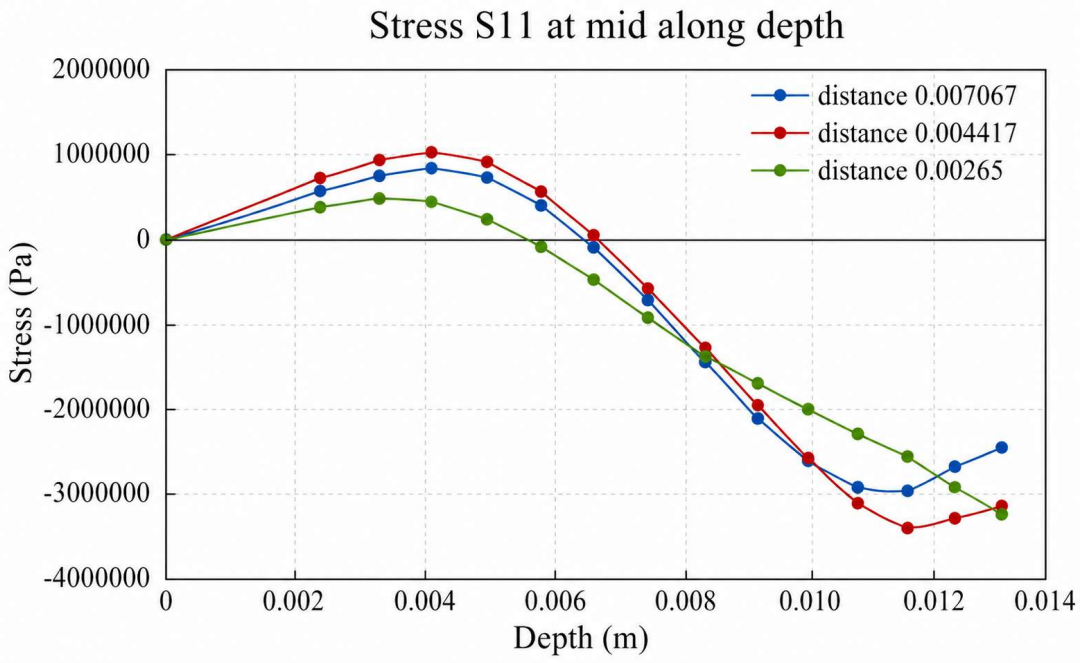

Figure 14. Stress in depth.

Figure 15 shows that the stress along the tip was highest in the area in front of the cooling path and lowest or zero at the corner. However, when any crack initiated at the maximum stress area, it released stress at that zone.

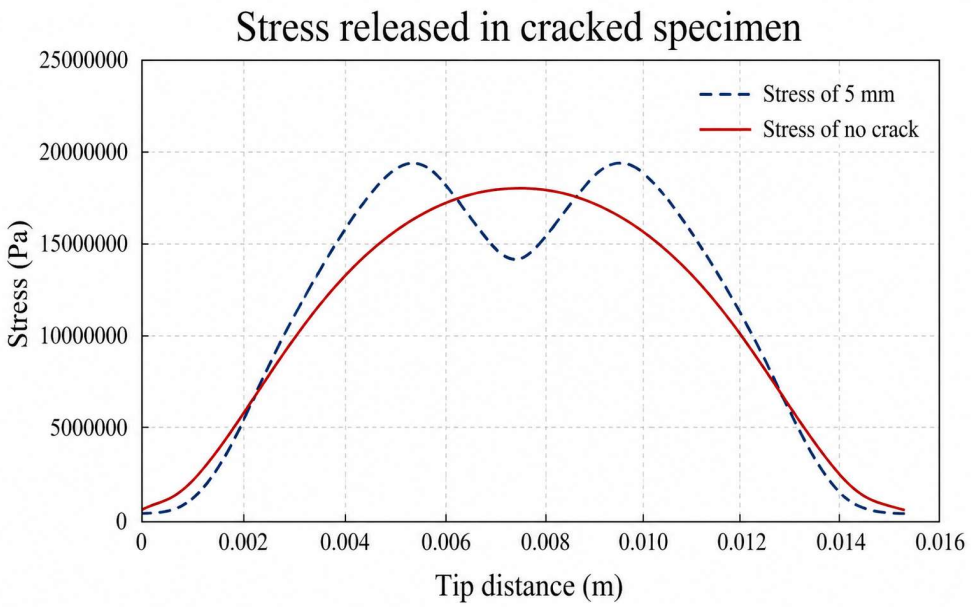

Figure 15. Stress releases in cracked specimens.

As the cracks propagate, stress release increases. When the stress value becomes very small at the crack tip, the crack stops propagating. Cracks release stress, and the energy release rate is directly proportional to the crack length. As the crack length increases, the value of J-integral also increases. Figure 16 shows the J-integral value at different crack lengths; the J-integral increased at 4 mm crack length; afterward, if crack length increased, J-integral decreased. This means that the crack can only be propagated to the length of 4 mm.

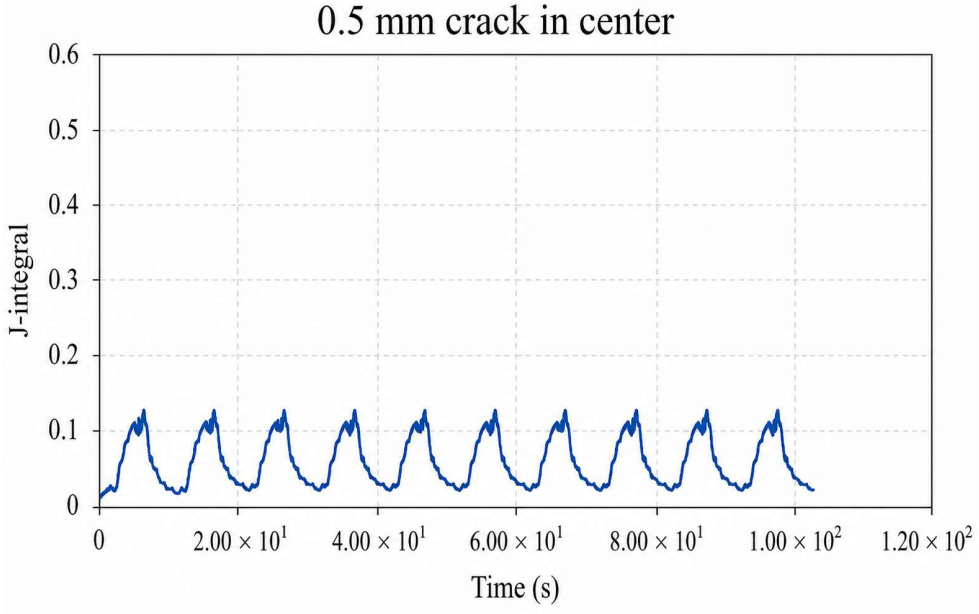

Figure 16. Curve between J-integral and time.

The J-integral represents the energy release rate associated with crack propagation; this value was evaluated to quantify the fracture behavior of the material under thermal fatigue loading. In the present study, the J-integral was estimated based on the relationship between crack length, stress distribution, and strain energy release within the specimen. The variation of J-integral with crack length was determined using the experimentally obtained stress profile and crack measurements, assuming a linear elastic fracture behavior in the crack propagation behavior. The J-integral was considered proportional to energy release and was evaluated as a crack length function using the corresponding stress-filed data obtained along the specimen tip.

In the present study, the increase in J-integral with crack length up to approximately 4 mm indicates an increasing driving force during the early propagation stage. Beyond this point, the observed decrease in J-integral suggests a reduction in the effective driving force; however, this alone does not imply crack arrest. The stabilization of crack growth rate observed experimentally is more appropriately attributed to a combination of factors, including thermal stress intensity due to stress redistribution, localized plastic deformation at the crack tip, crack interaction effects, and possible crack closure during cyclic thermal loading. Additionally, thermal fatigue conditions may introduce oxidation and microstructural degradation at the crack tip, which can further influence crack growth resistance. Therefore, the observed limitation in crack propagation is interpreted as a result of evolving balance between driving force and resistance under cyclic thermal loading, rather than a strict geometrical limit imposed by crack length alone.

Figure 17 shows the relationship between energy release rate and hundred cycle time. As the crack length increases to 4 mm, the energy release rate or J-integral value increases up to almost 4.00. When crack length increases from 4 to 5 mm, energy release rate decreases to 3.5.

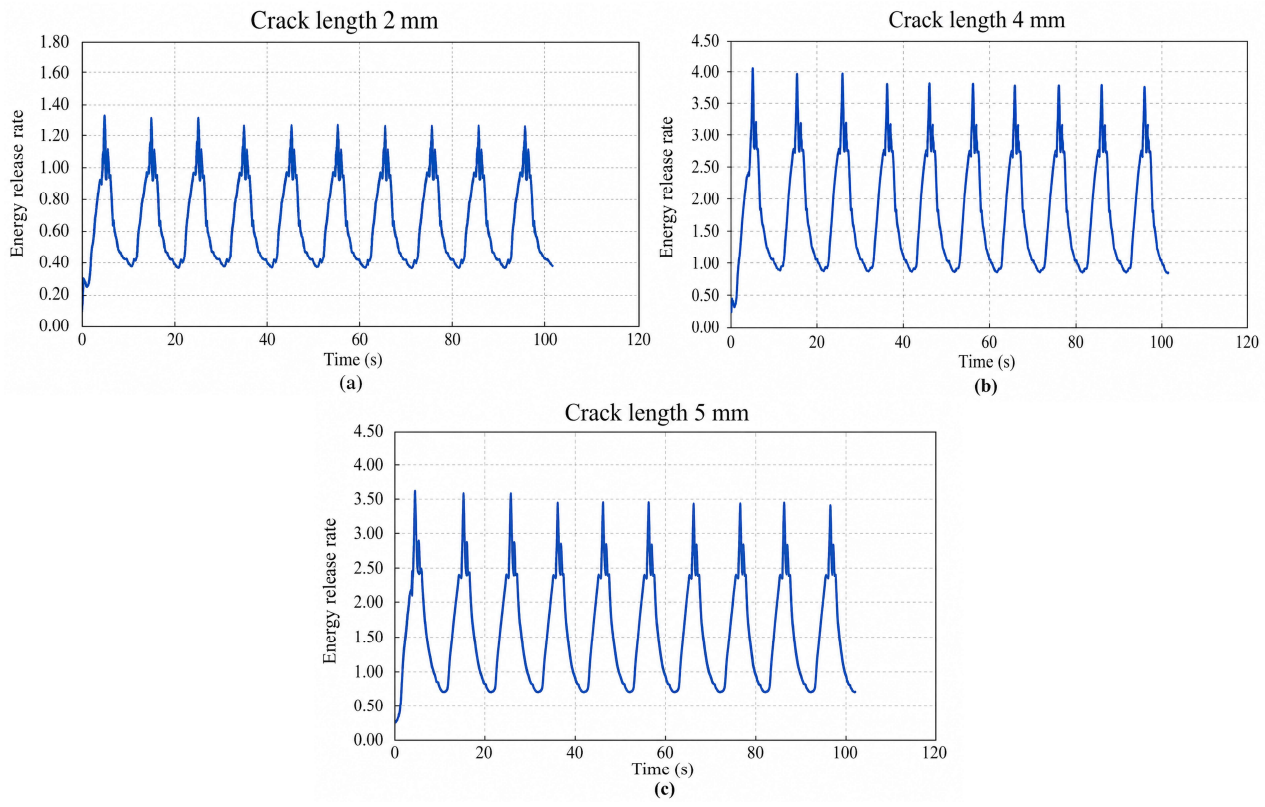

Figure 17. Crack from side 4.4 mm: (a) crack length 2 mm; (b) 4 mm; and (c) 5 mm.

To summarize, crack initiation life was defined as the first observation of a surface crack at the specimen tip with a measurable length ≥0.3 mm (300 μm), which corresponds to the practical optical detectability limit in this study. The specimen tip was inspected every 500 cycles, so the initiation-life resolution was limited by the inspection interval (±500 cycles). Crack length was measured from optical images using a calibrated length scale, and the crack-length measurement uncertainty was estimated to be ±10–20 μm.

4. Conclusions

An experimental investigation was conducted to evaluate the thermal fatigue behavior of cast Al4032 alloy under cyclic thermal loading conditions representative of automotive piston service. Based on experimental observations and measurements, the following conclusions can be drawn:

(1) Thermal fatigue cracking was experimentally observed to initiate after approximately 3000 thermal cycles under a temperature of 75–270 °C, indicating a distinct nucleation threshold under cyclic thermal gradients. Crack initiation consistently occurred near internally cooled regions, where the highest thermal gradients and stress concentrations were developed.

(2) Crack propagation was identified as the dominant damage stage at approximately 3000–15,000 cycles, during which crack length increased rapidly. Beyond this range, crack growth rate decreased significantly, leading to the saturation stage, where further increases in crack length became negligible.

(3) Stress analysis revealed that the maximum thermal stress was concentrated in regions located approximately 3.35–5.3 mm from the specimen edge, corresponding to zones directly influenced by internal cooling. The maximum stress along the specimen tip reached approximately 76.4 kPa, while lower stress levels (60 kPa) were observed at the central region, confirming on-uniform stress distribution.

(4) Crack propagation was found to be limited to a depth of 4.1 mm, beyond which compressive stress developed, restricting further crack growth. The energy release rate (J-integral) increased with rack length up to approximately 4 mm, after which it decreased, indicating a natural stabilization of crack propagation.

(5) Overall, the experimental findings confirm that Al4032 exhibits measurable resistance to thermal fatigue under cyclic thermal loading; however, prolonged exposure to severe thermal gradients leads to progressive crack development that may compromise structural integrity in piston applications.

(6) From an engineering perspective, the identified high-stress regions associated with internal cooling suggest that design optimization of cooling channel placement and geometry is critical for improving thermal fatigue resistance. Avoiding localized thermal gradients and stress concentration zones can significantly delay crack initiation and extend component life.

(7) The findings of this study are directly relevant to automotive piston applications, where there is cyclic thermal loading. The experimental insights provided in this work offer a more realistic understating of thermal fatigue behavior, contributing to improved durability design of aluminum piston alloys.

5. Future recommendations

Future work could use this experimental rig after the application of specific changes:

- New experiments can be conducted by increasing or decreasing heating and cooling times.
- Different materials can be used for the investigation of thermal fatigue on wedge-shaped specimens.

• Crack initiation and propagation analysis can be conducted on different heat-treated specimens to evaluate the effect of hardness on crack initiation.

• Simulations can be performed with primary and secondary cracks at the same time on wedge-shaped specimens.

• External water cooling can be used rather than internal cooling on wedge-shaped specimens for thermal fatigue life.

• A die casting process on casting specimens can be used for thermal fatigue analysis.

6. Limitations

• Casting was performed using conventional laboratory-scale sand casting; specific furnace and degassing details were not recorded.

• While minor mechanical effects arising from contact and fluid flow cannot be eliminated, their contribution is considered secondary. Future work may incorporate detailed thermo-mechanical analysis to quantify these effects.

• The reported crack initiation (3000 cycles) and crack saturation (15,000 cycles) values represent approximate observations under the tested conditions. For future work, a comprehensive statistical analysis including specimens per condition and standard deviation of crack initiation life is recommended.

• Although tensile testing was performed on an MTS 810 machine following the general procedure described in [35], the original test log did not retain the complete reporting parameters required for full reproducibility (e.g., specimen gauge length and cross-section, loading rate/strain rate, strain measurement method, test temperature, and number of repeat specimens). Similarly, hardness testing details (method/standard, load, dwell time, indentation mapping strategy, and statistical reporting) were not fully recorded. Therefore, the tensile/hardness values reported in this study should be interpreted as representative supporting measurements for the tested cast Al4032 condition rather than a statistically validated material-property dataset. Future work will implement standard-compliant reporting (e.g., full specimen geometry and test conditions, repeat specimens, and mean ± standard deviation) to strengthen statistical confidence and reproducibility.

• Temperature was measured at a single location near the specimen tip (~1 mm from the tip) primarily to control and repeat the thermal cycling waveform. Spatial temperature gradients across the specimen were not directly measured with multiple sensors in this study; therefore, gradient localization is interpreted using the imposed boundary conditions and the corresponding stress-field analysis. Multi-point thermocouple mapping and/or IR thermography will be implemented in future work to directly quantify the internal cooling–induced temperature field and further validate crack-initiation mechanisms.

Use of AI tools declaration

The authors declare they have not used Artificial Intelligence (AI) tools in the creation of this article.

Author contributions

Muhammad Arslan: conceptualization, methodology, formal analysis, investigation, validation, data curation, writing—original draft, writing—review & editing; Muhammad Zubair Farrukh:

conceptualization, methodology, formal analysis, investigation, writing—review & editing, and resources; Zaheer Uddin Kamran: formal analysis, methodology, writing—review & editing; Ahmed Usman Yasir: conceptualization, methodology, formal analysis, investigation, validation, data curation.

Data availability statement

The data supporting reported results are available in the manuscript.

Conflict of interest

The authors declare no conflict of interest.

References

1. Li T, Lu Q, Wang S, et al. (2025) Investigation on thermal fatigue properties of a grid-structured CoCrNi-Fe/Ni dissimilar coating fabricated by laser cladding. *Mater Today Commun* 49: 113979. https://doi.org/10.1016/j.mtcomm.2025.113979
2. Li CD, Yang HY, Dong BX, et al. (2025) Thermal fatigue failure mechanisms and enhancement strategies of die steel. *J Mater Res Technol* 38: 4567–4599. https://doi.org/10.1016/j.jmrt.2025.08.198
3. Liu X, Huang K, Zhou J, et al. (2025) Temperature effects on fatigue properties of plain-woven composites by an acoustic-optical-thermal multi-information fusion method. *Int J Fatigue* 193: 108757. https://doi.org/10.1016/j.ijfatigue.2024.108757
4. Gao Z, Cheng T, Zhang N, et al. (2025) Thermal-mechanical coupling simulation and experimental study of ultrasound-assisted laser cladding of Ni60 coating. *J Alloys Compd* 1024: 180270. https://doi.org/10.1016/j.jallcom.2025.180270
5. Patarić A, Djurdjevic M, Manasijevic S, et al. (2025) The role of silicon during solidification process of cast Al-Si-Mg alloys. *Materials* 18: 5033. https://doi.org/10.3390/ma18215033
6. Camargo OAB, Padilha GS, Pinto FC, et al. (2025) Synergistic effects of minor Be and Zr contents on microstructural and mechanical properties of A356 cast alloy. *Int J Metalcast* 19: 1676–1689. https://doi.org/10.1007/s40962-024-01416-3
7. Cheng X, Xiong B, Yu M, et al. (2025) Effect of grain characteristics on stress corrosion resistance of a novel Al-Mg-Zn-Si alloy with high Mg content. *Mater Today Commun* 46: 112413. https://doi.org/10.1016/j.mtcomm.2025.112413
8. Yan L, Xu H (2025) Lightweight composite materials in automotive engineering: State-of-the-art and future trends. *Alex Eng J* 118: 1–10. https://doi.org/10.1016/j.aej.2024.12.002
9. Vishnu SK, Rajeev VR (2024) Microstructure, hardness, and wear characteristics of eutectic and hyper eutectic Al-Si-Cu-Ni piston alloys, In: Singh S, Singh I, *Advances in Materials and Manufacturing. ICDMT 2024. Lecture Notes in Mechanical Engineering*, Singapore: Springer. https://doi.org/10.1007/978-981-96-7659-0_19
10. Tommy SD, Onah TO, Aneke AC (2025) Ageing on mechanical and microstructural properties of aluminum-silicon metal matrix composites: A review. *World J Adv Res Rev* 27: 535–547. https://doi.org/10.30574/wjarr.2025.27.1.2507

11. Ozbek YY, Yeşil F (2025) Fatigue behavior of aluminum alloys produced by high-pressure die casting method. *Inter Metalcast*. https://doi.org/10.1007/s40962-025-01700-w
12. Hu P, Pan L, Chen XG (2024) Elevated-temperature performances of Al-Si-Cu casting alloys for cylinder head applications. *Mater Charact* 218: 114484. https://doi.org/10.1016/j.matchar.2024.114484
13. Ziadoon AH, Al-Khazraji AN, Shandookh AA (2025) Investigation of creep behaviour of metal functionally graded materials. *AIP Conf Proc* 3350: 050020. https://doi.org/10.1063/5.0297420
14. Angeloni M, Ruchert COTR, Bose Filho WW, et al. (2025) Fatigue life assessment of A356 aluminium alloy used for engine cylinder head. *J Braz Soc Mech Sci Eng* 47: 175. https://doi.org/10.1007/s40430-025-05487-z
15. Zhang C, Liao W, Shan Z, et al. (2024) Squeeze casting of 4032 aluminum alloy and the synergetic enhancement of strength and ductility via Al-Ti-Nb-B grain refiner. *Mater Sci Eng A* 896: 146233. https://doi.org/10.1016/j.msea.2024.146233
16. Tian H, Ma DM, Zhao X, et al. (2025) Effect of double deformation extrusion on the microstructure and properties of 4032 aluminum alloy. *Mater Today Commun* 42: 111396. https://doi.org/10.1016/j.mtcomm.2024.111396
17. Baharudin A, Purwanto W, Setiawan MY, et al. (2025) Coupled thermo-structural simulation of Al2618, Al4032, and Al6061 pistons in a single-cylinder diesel engine. *MOTIVECTION J Mech Electr Ind Eng* 7: 229–244. https://doi.org/10.46574/motivection.v7i2.471
18. Ghoujehzadeh A, Mohtadi-Bonab MA, Jahani D (2025) Optimization and finite element analysis of an aluminum piston in the Peugeot XU7JPL3 engine for enhanced efficiency and durability. *Discov Mech Eng* 4: 6. https://doi.org/10.1007/s44245-025-00091-w
19. Kumar NS, Pramod GK, Samrat P, et al. (2022) A critical review on heat treatment of aluminum alloys. *Mater Today Proc* 58: 71–79. https://doi.org/10.1016/j.matpr.2021.12.586
20. Singh AB, Singh S, Dangayach GS, et al. (2023) Fatigue behavior analysis of EN8 steel subjected to various heat treatments created for shaft. *Mater Today Proc*. https://doi.org/10.1016/j.matpr.2023.02.165
21. Azadi M, Shirazabad MM (2013) Heat treatment effects on thermo-mechanical fatigue and low cycle fatigue behaviors of A356.0 aluminum. *Mater Des* 45: 279–285. https://doi.org/10.1016/j.matdes.2012.08.066
22. Ilman MN (2014) Chromate inhibition of environmentally assisted fatigue crack propagation of aluminum alloy AA2024-T3 in 3.5% NaCl solution. *Int J Fatigue* 62: 228–235. https://doi.org/10.1016/j.ijfatigue.2013.03.008
23. May A, Belouchrani MA, Taharboucht S, et al. (2010) Influence of heat treatment on the fatigue behavior of two aluminum alloys 2024 and 2024 plated. *Procedia Eng* 2: 1795–1804. https://doi.org/10.1016/j.proeng.2010.03.193
24. Paffumi E, Nilsson KF, Szaraz Z (2015) Experimental and numerical assessment of thermal fatigue in 316 austenitic steel pipes. *Eng Fail Anal* 47: 312–327. https://doi.org/10.1016/j.engfailanal.2014.01.010
25. Mellouli D, Haddar N, Koster A, et al. (2014) Hardness effect on thermal fatigue damage of hot-working tool steel. *Eng Fail Anal* 45: 85–95. https://doi.org/10.1016/j.engfailanal.2014.06.007
26. Zhang Q, Zuo Z, Liu J (2014) Stepped-isothermal fatigue analysis of engine piston. *Fatigue Fract Eng Mater Struct* 37: 417–426. https://doi.org/10.1111/ffe.12125

27. Arabacı U, Karacif K, Albayrak S, et al. (2025) Effect of heat treatment on corrosion and wear properties of powder metal AZ91 magnesium alloy. *Mater Test* 67: 1924–1937. https://doi.org/10.1515/mt-2025-0208
28. Park CW (2013) The development of aluminum alloy piston for two-stroke cycle engines by powder forging. *J Korean Soc Manuf Technol Eng* 22: 173–177. https://doi.org/10.7735/ksmte.2013.22.1.173
29. Alshoaibi AM, Fageehi YA (2024) Advances in finite element modeling of fatigue crack propagation. *Appl Sci* 14: 9297. https://doi.org/10.3390/app14209297
30. Bhattachar VS (1995) Thermal fatigue behaviour of nickel-base superalloy 263 sheets. *Int J Fatigue* 17: 407–413. https://doi.org/10.1016/0142-1123(95)00006-F
31. Amiable S, Chapuliot S, Constantinescu A, et al. (2006) A computational lifetime prediction of a thermal shock experiment. Part I: Thermomechanical modelling and lifetime prediction. *Fatigue Fract Eng Mater Struct* 29: 175–182. https://doi.org/10.1111/j.1460-2695.2006.0976.x
32. Szmytka F, Salem M, Rezai-Aria F, et al. (2015) Thermal fatigue analysis of automotive diesel piston: Experimental procedure and numerical protocol. *Int J Fatigue* 73: 48–57. https://doi.org/10.1016/j.ijfatigue.2014.11.011
33. Edalat Nobarzad AK (2017) Influence of microstructure on susceptibility to weld defects in two high strength low alloy steels. Doctoral dissertation, Ecole de Technologie Supérieure.
34. Girisha VA, Joshi MM, Kirthan LJ, et al. (2019) Thermal fatigue analysis of H13 steel die adopted in pressure-die-casting process. *Sādhanā* 44: 148. https://doi.org/10.1007/s12046-019-1111-3
35. Hormozi R, Biglari F, Nikbin K (2015) Experimental study of type 316 stainless steel failure under LCF/TMF loading conditions. *Int J Fatigue* 75: 153–169. https://doi.org/10.1016/j.ijfatigue.2015.02.014
36. Karl J (2013) Thermomechanical fatigue life prediction of notched 304 stainless steel. Master's thesis, University of Central Florida. Available from: https://stars.library.ucf.edu/etd/2645.

AIMS Press